Functionalized Graphene and Applications

İlhan A. Aksay
İlhan A. Aksay, born in Paşabahçe, İstanbul, is a dual citizen of Türkiye and the United States of America. After graduating from Vefa Lisesi in İstanbul (1962), he earned his B.Sc. (1967) in ceramic engineering at the University of Washington, Seattle, and M.Sc. (1969), Ph.D. (1973) in materials science and engineering at the University of California, Berkeley. Prior to joining Princeton University in 1992, his teaching and research affiliations included appointments at the University of Washington, Seattle (1983-92); University of California, Los Angeles (1981-83); the Middle East Technical University, Ankara, Türkiye (1975-81); and Xerox Corporation, Webster Research Center, Webster, New York (1973-75). He is now the Pomeroy and Betty Perry Smith, Emeritus Professor in the Department of Chemical and Biological Engineering of Princeton University. He is a member of the U.S. National Academy of Engineering, NAE (2010), the Science Academy, Türkiye (2012), and the U.S. National Academy of Inventors, NAI (2014). He is also a Fellow of the American Association for the Advancement of Science (AAAS), the American Ceramic Society, and an honorary member of the Japanese Materials Research Society. He received the Richard M. Fulrath (1987) and the Edward C. Henry (2000) Awards of the American Ceramic Society, the Charles M. A. Stine Award of the American Institute of Chemical Engineers (1997), and the Turkish National Medal of Science (Tübitak) (2001). In recognition of his research and efforts in promoting technology transfer, he was named the Puget Sound (Washington State) Engineering Council's 1988 Academic Engineer of the Year.

By: İlhan A. Aksay

https://doi.org/10.51167/acm00060

GRAPHENE HAS BEEN THE RISING STAR of condensed-matter physics and materials science during the last two decades with many promising applications.[1] Functionalized graphene produced by the thermal[2,3] or solvent[4] exfoliation and reduction of graphite oxide (GO) has also been on the rise and has found numerous applications in polymer composites,[5,6] electrical energy and storage devices,[7-15] electrochemical sensors,[16-19] photovoltaics,[20-23] catalytic combustion of fuels,[24-28] colloidal suspensions[29-31] and tapes[32] for electromagnetic shielding[33-35] and corrosion prevention,[36,37] and iron-on components, such as antennas,[38,39] for wearable electronics. What makes functionalized graphene suitable for this wide range of uses is the fact that it combines electrical conductivity with a large number density of oxygen-containing functional groups and lattice defects.[40,41]

I contend that the defective and functionalized forms of graphene, with variations in its chemistry and structure, are as invaluable and critical as pristine graphene, not only for condensed-matter physics, but also for chemistry, materials science, biology, and engineering. The validity of this contention has already been demonstrated in numerous applications listed above.

In the following sections on the (i) Production of functionalized graphene by thermal exfoliation, (ii) Chemistry and structure of functionalized graphene, (iii) Electrical properties, (iv) Applications, and (v) Prospects, I review the contributions to the functionalized graphene field, with emphasis on thermal exfoliation and reduction of GO, and provide examples where it is more appropriate to use functionalized graphene.

Production of functionalized graphene by thermal exfoliation

Steps leading to our work on the processing of functionalized graphene started, before our time, with Benjamin Brodie in England and his seminal paper published in 1859.[42] Brodie, in his studies on the acid treatment of graphite, produced an oxidized form of graphite with a C/O of ~2.[42,43] He referred to this material as graphic acid; but, a more descriptive name "graphite oxide" GO caught on instead. The first effort to exfoliate GO was in 1898 by Staudenmaier[44] in Germany. Brodie's and Staudenmaier's studies were conducted even before the crystal structure of graphite was determined by Bernal in 1924.[45] Hummers and Offeman introduced an improved and safer oxidation method to produce GO in 1958.[46,47] Only in 1962, Boehm et al.[48] showed that GO deflagrates at 200-325°C on rapid heating with the formation of light and voluminous black flakes (soot). They stated (with caution) that some single sheets may have formed. The first convincing demonstration of the reduced forms of single sheet graphene oxide by the Staudenmaier's oxidation method was reported in our 2006 and 2007 publications (Figure 1).[2,3] We demonstrated that the thermal expansion method, when optimized, indeed leads into the formation of reduced and electrically conducting graphene oxide sheets, with C/O values around 10 then, and now with C/O values as high as a few hundreds.[10,14,49]

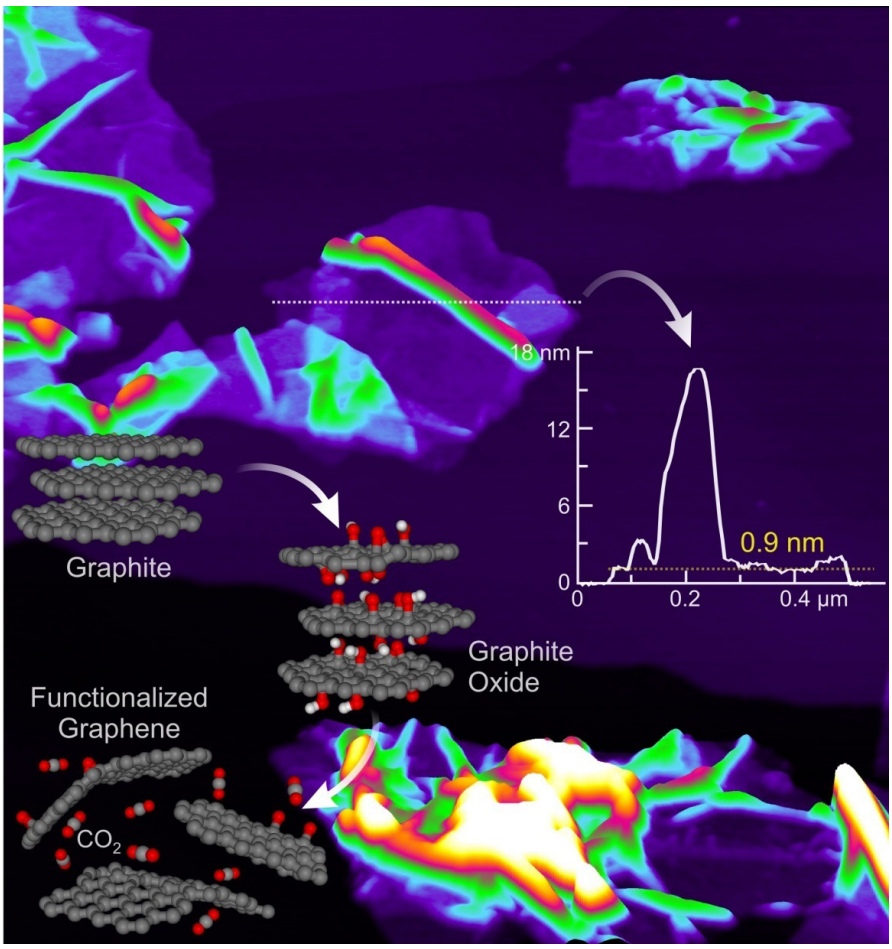

Figure 1.[3] Schematic representation of the Brodie and Staudenmaier methods. Starting with the graphite particles, graphite oxide (GO) is produced by acid treatment. Dry graphite oxide particles are rapidly (2000°C/min) heated to 1050°C to expand them to single sheets of reduced GO particles (purple, green, red, yellow regions in the tapping-mode atomic force microscopy (AFM) images of functionalized graphene sheet (FGS) deposited on a freshly cleaved highly oriented pyrolytic graphite (HOPG) surface. AFM height profile along the dashed line shows that the purple color parts of these sheets, on the average, are 0.9 nm in thickness. There can be only one reduced GO sheet in these purple regions as the thickness of a single GO sheet is 0.6-0.7 nm thick. Colors ranging from green to red and bright yellow correspond to much larger heights indicating a crumpled sheet structure.

Realizing that what we produced is not a defect-free and chemically-pure graphene, we coined this form of reduced graphene oxide as functionalized graphene sheet (FGS) to distinguish it from pristine graphene (Figure 1).[3] We also indicated its C/O ratio with a subscript x at the end as FGS_x. FGS_2 designates the basal plane of Brodie's material; FGS_{10} is the single sheet produced by the thermal expansion and reduction method. FGS_2 is an electrical insulator; FGS_{10} is an electrical conductor.[49] The rapid heating method is not just an expansion process, but also a partial reduction technique to regain pristine graphene's most important property, high (ballistic) mobility of its charge carriers.[50]

Our own preference of the thermal expansion of GO method at the 1050-1100°C range is due to two reasons: (i) to make sure the exfoliation to single sheets indeed takes place, and (ii) being able to increase the C/O ratios to much higher values (>500). Flexibility to change the C/O value by two orders of magnitude is a major challenge for solvent based methods, but not for thermal expansion. The reduction can be done by simply increasing either the residence time during the thermal expansion or with additional post heat treatment. By tuning the C/O, a whole family of functionalized graphenes can be produced with a broad spectrum of physical and chemical properties: On one end of the spectrum lies graphene oxide with a C/O of 1.8[51] to 2.3[52] depending on the synthesis and characterization protocol.[53] That is an electrical insulator[54] since most of the carbon atoms are sp^3 hybridized[55] and remains so until the C/O exceeds ~7.[49] Pristine graphene lies on the other end of the spectrum. It exhibits the smallest density of defects. Yet, in some applications such as electrochemical double layer capacitors (supercapacitors or ultracapacitors), the presence of functional groups and defects provides a large electronic density of states to increase the surface-specific capacitance of FGSs by a factor of ~4 compared to pristine graphene.[14] Thus, it is better to use a reduced form of graphene oxide in such cases, rather than pristine graphene.[14]

In GO preparation, the complete oxidation of graphite is a critical step. We define complete oxidation of graphite by the total

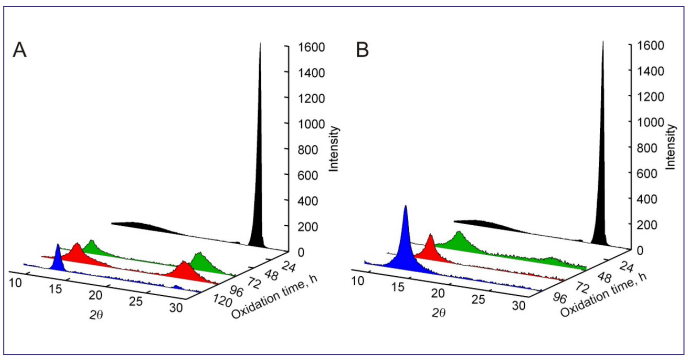

Figure 2.[3] **(A) X-ray diffraction (XRD) patterns of 400 µm diameter graphite flakes oxidized for various lengths of time. Note that the native graphite peak (between 2Θ of 25-30°) persists for oxidation times as long as 96 h. A new peak corresponding to an interlayer spacing of 0.7 nm forms during the oxidation. (B) XRD patterns of 45 µm diameter graphite flakes oxidized for various lengths of time. Note the disappearance of the native graphite peak after relatively shorter (72 h vs. 120 h) oxidation times.**

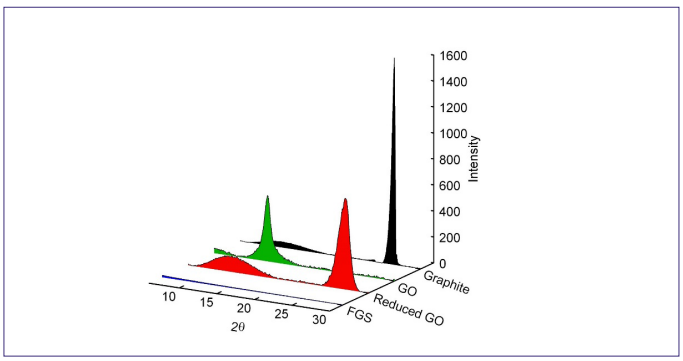

Figure 3.[3] **XRD patterns of graphite, GO, GO that has been thermally reduced by slow heating (1 °C/min), and FGS. When GO is heated slowly, the rate of gas evolution is insufficient to yield high enough pressures to overcome the van der Waals attraction between the layers, and with the removal of the functional groups the layers re-stack to roughly the initial graphite spacing. FGS displays an amorphous diffraction pattern.**

disappearance of the 0.34-nm intergraphene spacing and the appearance of a new peak with a 0.65-0.75 nm range depending on the water content of GO, as determined by X-ray diffraction (XRD) (Figure 2).[3] The size of the graphite particles is a critical variable in determining the complete oxidation time. As shown in Figure 2B,[3] while 45 µm size graphite particle oxidation is completed after 96 h, with 400 µm particles it takes up to 120 h. The disappearance of the 0.34 nm spacing between the 0001 planes of graphite has been reported previously;[56] but, GO with such characteristics has never been reported in thermal expansion studies, which is an essential step for a successful splitting of GO into single functionalized graphene sheets.

The purpose of the rapid heating rate is to overwhelm the process by rapid decomposition rates vs. the diffusion rates of the evolved gases through interstices. The exfoliation of GO is due to the pressure build up as CO_2 (and some CO) gas evolves into the interstices between the 0001 planes (Figure 1).[3] With slow heating rates or by annealing at low temperatures, CO_2 will diffuse through the interstices (Knudsen diffusion) at a faster rate than the gas formation rate by decomposition; thus, without building up high enough pressures to expand the GO.[3] Further, while the decomposition of the functional groups of GO yielding CO_2 is exothermic, the vaporization of water is endothermic and delays the heating process. For the success of the process, these are the two key reasons why high heating rates are critical to move into the decomposition dominated regime at higher temperatures rapidly.[3] Otherwise, the end product will

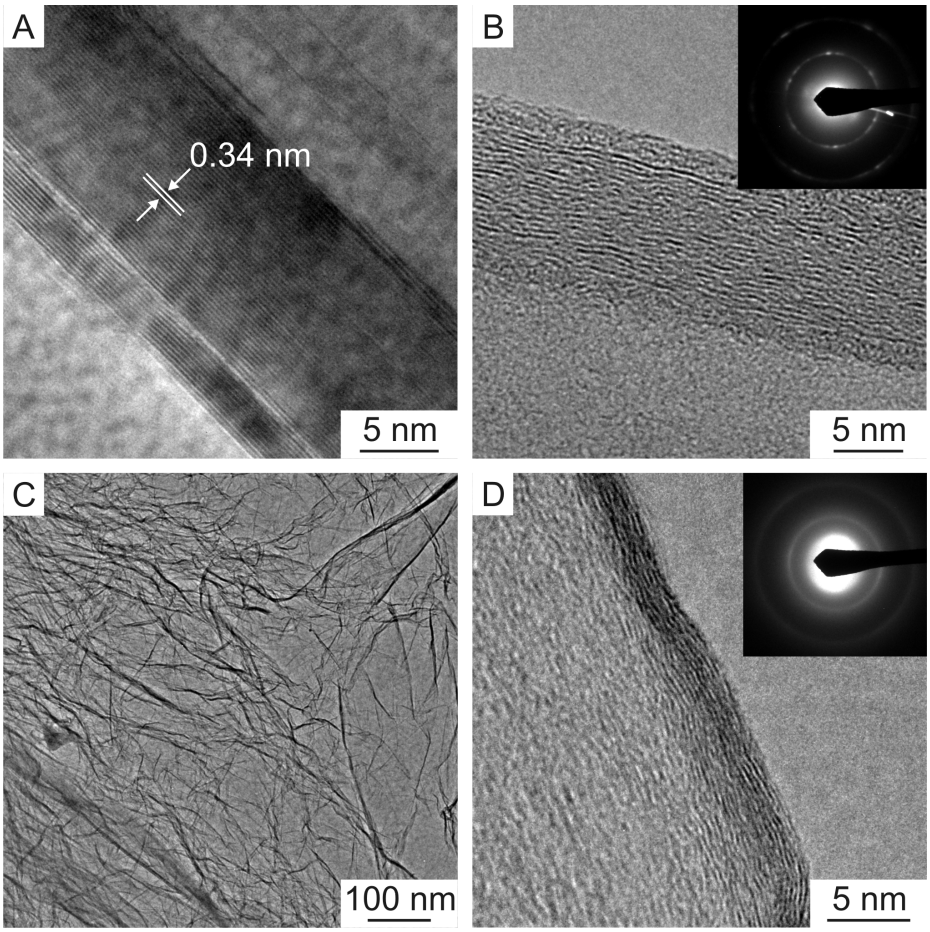

Figure 4.[3] **(A) High resolution transmission electron microscopy (HRTEM) image of graphite showing its characteristic 0.34-nm interlaminar spacing. (B) HRTEM image illustrates the intercalation of GO samples oxidized for more than 96 h. The GO sheets are wrinkled compared to that of pristine graphite. The selected area electron diffraction (SAED) pattern in the inset containing information from many GO grains. (C) TEM image of FGS. (D) An edge-on HRTEM image of FGS produced from GO with a 96-h acid treatment showing a multi-stack region to illustrate that even in our own work, trace amounts of stacked up graphene oxide regions exist.**

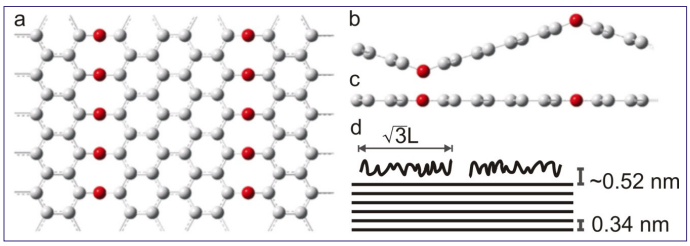

Figure 5.[59] (a) A partially oxidized graphene sheet containing epoxy strings in planar view prior to the tensile deformation; oxygen and carbon atoms are shown in red and grey, respectively. (b) An edge view of (a); epoxy lines cause the sheet to undulate. (c) The sheet is completely flattened upon the application of tensile strain. (d) Schematic of undulation and crack formation on the uppermost graphene oxide sheet. (a)-(c) are provided by K.N. Kudin.[58]

only be reduced GO without expansion, instead of the single sheets of reduced graphene oxide (FGS) as shown in Figure 3.[3] A survey of the literature shows that in many publications this issue is overlooked and assumed that GO is indeed not only reduced but also exfoliated.

Chemistry and structure of FGS

An NMR study[57] has shown that GO as used in the thermal exfoliation process contains aromatic regions randomly interspersed with oxidized aliphatic six-membered rings. The oxidized rings contain C-O-C (epoxide) and C-OH groups, while the sheets terminate with C-OH and -COOH groups.[2,3,40,41] As a result of the intercalation of the acidic solution into graphite and the formation of these groups, structural changes take place as graphite transforms to GO. The first change is the increase in the interplanar distance between the 0001 planes from 0.34 to 0.65-0.75 nm range as demonstrated in the previous section with the XRD data of Figures 2 and 3.[3] In Figures 4A and B,[3] the high-resolution transmission electron microscopy (HRTEM) images also confirm this increase. A second structural change observed in Figure 4B is that the graphite oxide's 0001 planes are now undulated.[3] While the increase in the separation distance between the 0001 planes is partially due to the formation of the hydroxyl groups as depicted in Figure 1, the transitioning of the flat 0001 planes to an undulated morphology is caused by the kinking of the planes as the epoxide strings form.[58] This is because the equilibrium state of a C-O-C bond requires kinking (Figure 5).[58,59]

A third structural change is the cracking of the 0001 planes during the oxidation (Figure 6)[59] to allow kinking and thus the undulated morphology seen in Figure 4B. However, initially the flat planes of graphene oxide are not allowed to kink and shrink, as they are attached to the planes underneath by the van der Waals forces; thus, they experience elastic stresses while flat. To relieve this stress, the 0001 planes periodically crack, undulate, and shrink as shown in Figures 5 and 6.[59] The size distribution of the cells formed by cracking does not change significantly with oxidation time indicating that oxidation on an exposed surface reaches equilibrium rapidly. Penetration of the acid solution into the bulk through the cracks and the intercalation are the slow processes.[59] The oxidation process continues by a layer-by-layer cracking and intercalation process. Mechanistically, this process of periodic cracking is akin to a well-known process in periodic cracking commonly observed in thin films of brittle coatings and also in mud-cracking of drying lake beds.[60]

Structural and chemical changes continue through the heat treatment. GO to FGS transformation leaves behind topological defects and vacancies.[2,3] Some of the functional groups (C-O-C, C-OH groups and at the edges C-OH, -COOH groups) are retained in the thermally exfoliated and reduced graphene oxide sheets. The thermal reduction of GO removes both C and O atoms as CO_2 and CO evolve, creating carbon vacancies in the graphene lattice which are subsequently functionalized with ethers, hydroxyls, and carbonyls that saturate the sp^2 dangling bonds present at the vacancy edges.[2,3,40] Similar results were also reported in reactive field molecular dynamics (MD) simulations of thermally reduced graphene oxide.[41] Among the lattice vacancies, one of the more stable ones is the double vacancy (C2), which is composed of two pentagonal rings and one octagonal ring and is usually referred to as the 5-8-5 defect, Figure 7.[61,62] In addition to such 5-8-5 defects, 5-7-7-5 rings (the so-called Stone-Wales (SW) defects)[63] also play an important role in carbon nanotubes and other graphitic materials.[62] Note that, as shown in Figure 7b, these lattice defects also contribute to the formation of undulations in FGS. Thus, more wrinkling is expected with increasing C/O, except at very high C/O values (>500) when FGS is approaching a pristine graphene like state.

A demonstration of the points made so far is in Figure 8[10] with single layers of FGS_2, FGS_{13}, and FGS_{386} on gold and highly oriented

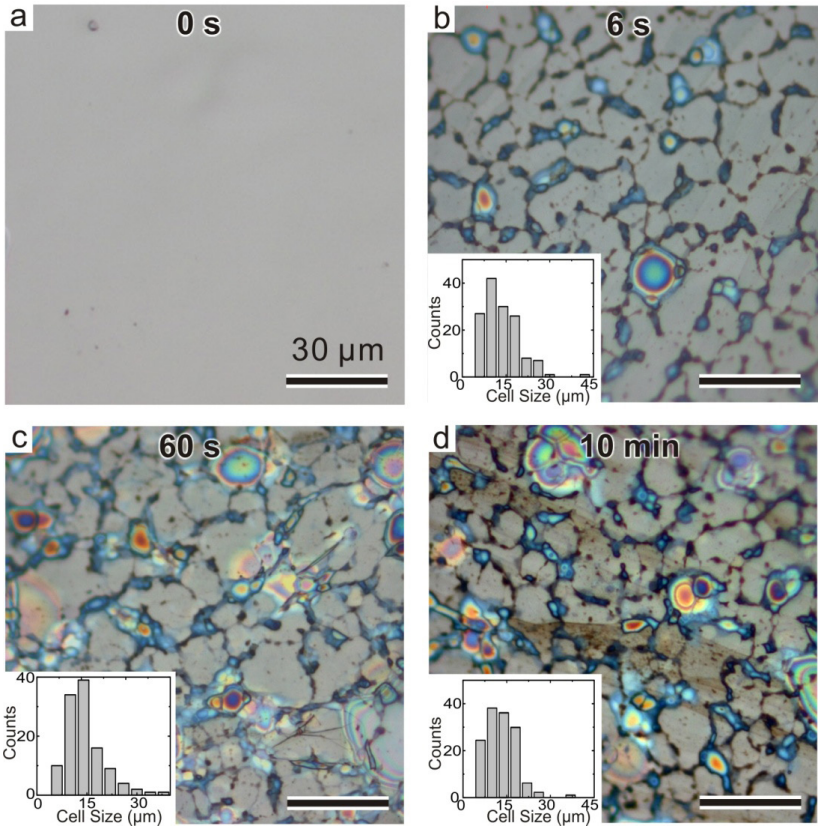

Figure 6.[59] Bright-field optical microscopy images of (a) HOPG prior to oxidation showing a featureless surface with no cracks, (b) after oxidized through acid treatment for 6 s, (c) 60 s, and (d) 10 min. Insets in b, c, and d are the histograms of respective cell sizes. All scale bars are 30 mm.

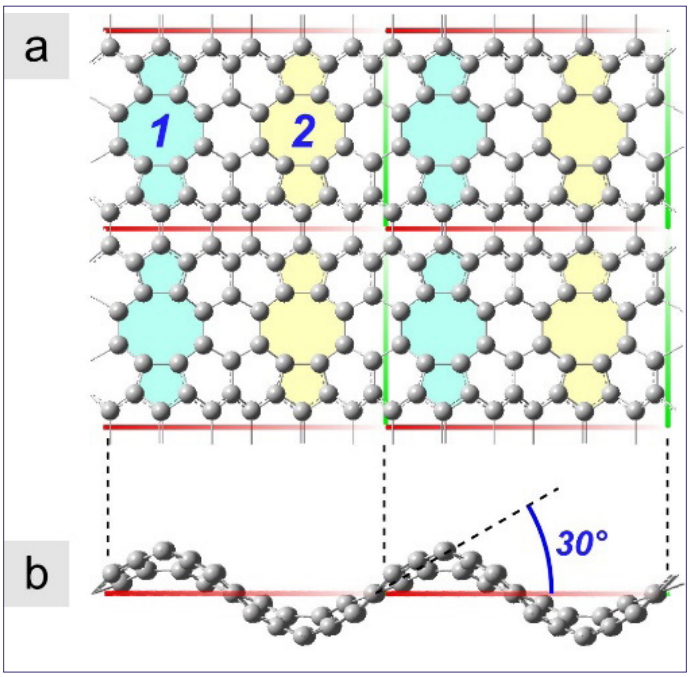

Figure 7.[61] Pattern of 5–8–5 defects in graphene organized in linear fashion. (a) Top view of 2×2 unit cells with two defects, each. (b) The side view shows that the two defect lines introduce kinks in the sheet. The defects are organized such that the bending of defects "1" (light cyan) is compensated by the bending of defects "2" (light yellow), so that a flat sheet results on surfaces. (refs)

pyrolytic graphite (HOPG) substrates.[10] Consistent with what has been presented, single sheets of FGS with a wide range of C/O values can be produced with the thermal expansion approach. Also, consistent with the changes discussed above, the sheet roughness is more noticeable as the C/O value increases, up to a limit above which healing towards pristine graphene like structure is expected.

To characterize the degree of reduction of FGS, we rely on Raman spectroscopy, especially considering the fact that conjugated and double carbon-carbon bonds lead to high Raman intensities.[40] Highly ordered graphite has only a couple of Raman-active bands visible in the spectra (Figure 9)[40]. The first one is due to the in-plane oscillations of any sp^2 carbon pair in the graphite lattice (G band) at 1580 cm^{-1}. The other one is the (weak) disorder band caused by the graphite edges (D band) at approximately 1355 cm^{-1}.[40,64] The D-peak is the result of the breathing mode of aromatic rings with sixfold symmetry.[64] However, this mode is only active in the presence of lattice disorder and thus the peak intensity also depends on the characteristic distance between defects or, alternatively, can be thought of as the average lateral crystallite size of pristine graphene domains.[65] Along the graphite-GO-FGS path, the Raman spectra undergo changes (Figure 9) that are similar to those observed in the graphite to amorphous carbon transition.[64] Specifically, the G band broadens significantly and displays a shift to higher frequencies (blue-shift), and the D band grows in intensity.[40] A notable fact is that while the G band peak is located at a higher frequency in GO than that in graphite (1593 vs. 1580 cm^{-1}), in FGS, it is back to almost the same frequency as that in graphite.

Figure 10A[14] summarizes the results from elemental analysis and Raman spectroscopy performed on a series of FGSs exfoliated and/or annealed at temperatures ranging from 300 to 2100°C. The change in the relative intensities of D and the G peaks (I_D/I_G) (Figure 10B) gives information about the changes in the structure of the sp^2 phase that evolves in between the defective regions after different reduction and annealing treatments.[64] Visible Raman spectroscopy does not give information about the sp^3 carbon content or the relative number of functional groups bound to the FGSs because the sp^2 signals are thought to be resonantly enhanced and effectively drown out any sp^3 contributions to the spectrum.[64] As shown in Figure 10B, we follow these changes by determining the C/O of the FGSs after the various reduction and annealing conditions. The C/O after thermal exfoliation increased from ~4 to 20 with increasing temperature. This corresponds to an approximate range of oxygen concentrations of 20 to 5 % (mol/mol) if only carbon and oxygen are considered (i.e., neglecting hydrogen). The C/O increases further to 180 and then to ~400 as the material was heat treated at higher temperatures for 2 h. The removal of oxygen partially restores the aromatic network, as indicated by the increase in sheet conductivity.[49]

Consistent with the Raman spectroscopy results, the scanning tunneling microscopy (STM) topography image of an FGS_{10}, (Figure 11)[40] taken on top of a wrinkle of the sheet shows a disordered structure in comparison to an STM image of a HOPG) surface (the inset on the left bottom) taken under identical conditions. However, the Fourier transform of the FGS image shows that the hexagonal order of graphene is still present (inset on the right top of Figure 11) in support of the data presented in Figures 9 and 10. Chemical information presented by

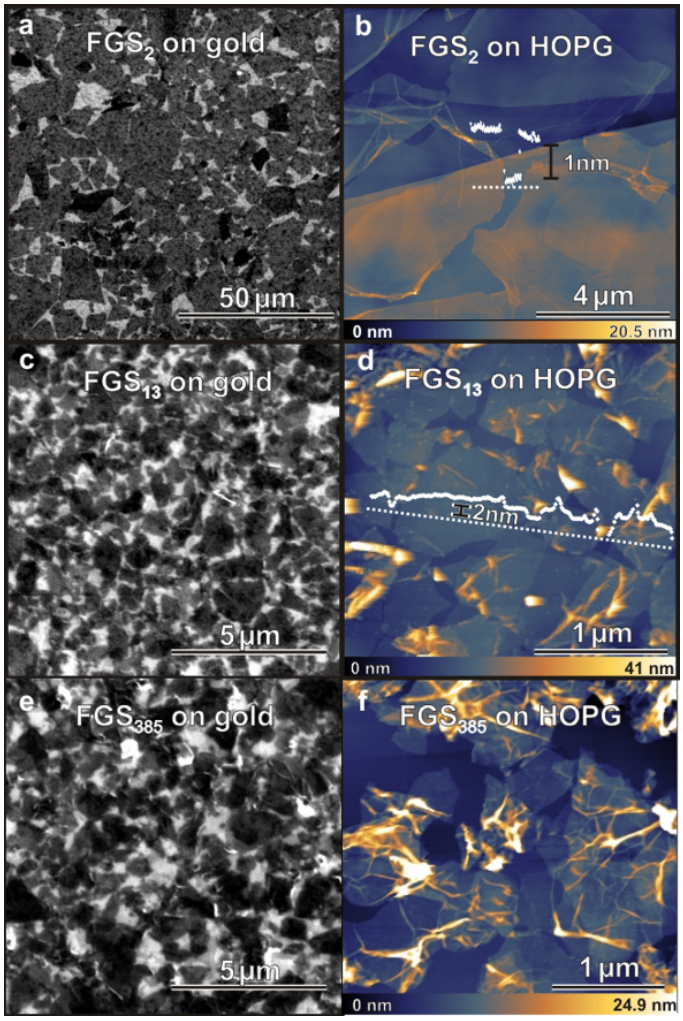

Figure 8.[10] Morphology of FGSs on gold and HOPG substrates: (a) Scanning electron microscopy (SEM) image of FGS_2 on gold; (b) tapping-mode AFM image of FGS_2 on HOPG; (c) SEM image of FGS_{13} on gold; (d) tapping-mode AFM image of FGS_{13} on HOPG; (e) SEM image of FGS_{385} on gold; and (f) tapping-mode AFM image of FGS_{385} on HOPG.

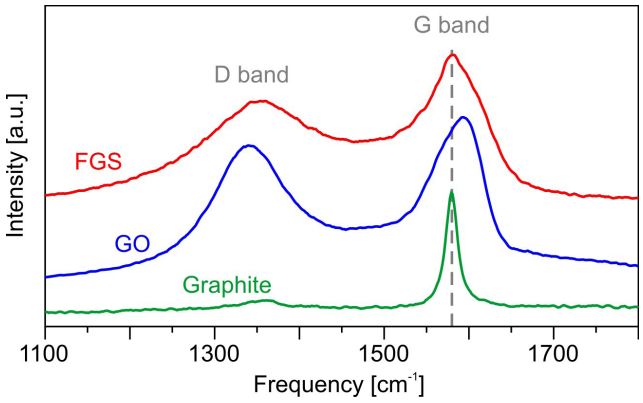

Figure 9.[40] **Evolution of the Raman spectra during the oxidation and exfoliation processes for graphite, GO, and FGS. All of the spectra correspond to an exciting laser wavelength of 514.5 nm. The position of the G band peak in graphite is indicated by a vertical, dashed line.**

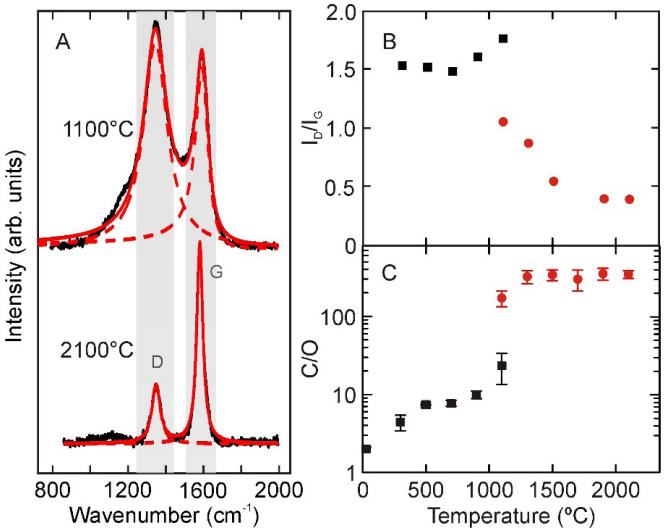

Figure 10.[14] **Estimating the degree of functionalization and defectiveness of FGSs. (A) Comparing the Raman spectra of FGSs treated at 1100 °C (above) and 2100 °C (below) showing D and G peaks ubiquitous in graphitic materials. Dashed red lines indicate the Lorentzian fit to the D-peak and the BWF fit to the G-peak and the solid red line is the sum of the two fits. (B) Ratio of the integrated ID to IG intensities as a function of heat treatment. Black squares were exfoliated at the indicated temperature for 60 s and red circles are for FGS that was exfoliated at 1100 °C for 60s that was further heat treated in a graphite furnace at the indicated temperatures for 1 h.**

C/O or the Raman spectroscopy I_D/I_G numbers are two quick ways to determine the degree of order induced back into the FGS.

To sum up, the physical features of the FGS demonstrated so far are: (i) They are only a few micron size sheets much smaller than the starting 45 to 400 µm size graphite particles (Figure 2); (ii) The sheets are undulated and wrinkled (Figures 1,6,8); (iii) Wrinkling and undulations are much less noticeable in FGS_2 vs. higher C/O versions (Figure 8). The crumpled nature of the FGS is helpful in preventing the re-graphitization of the FGSs by inhibiting layering of one FGS onto another.[66] This also helps to prevent layered aggregation between sheets in colloidal suspensions.[31]

Electrical Properties

We performed systematic studies on the electrical sheet resistance of FGSs ranging from $FGS_{7.2}$ to FGS_{349} based on both I/V curves from 2-probe measurements (including contact resistance) (Figures 12,13)[49] and on Kelvin probe force microscopy (KPFM) (excluding contact resistance).[49] With increasing C/O, FGS undergoes a transition from high-resistance (>400 kΩ/sq for a C/O of 7.3) with pronounced non-ohmic current/voltage (I/V) characteristics to low resistance (less than 10 kΩ/sq for a C/O of 340) with ohmic behavior. These measurements demonstrate that the electric conductivity of FGSs can be tuned in a wide range and, for the largest degree of reduction. The conductivity of FGS, by far, exceeds the conductivity of chemically reduced graphene oxide and of graphene oxide reduced thermally on substrates.[49] In contrast, pristine graphene (highly doped or biased) displays electrical sheet resistance below 1 kΩ/sq.[49]

Applications

In many applications, FGS powder itself is the final commercial product with the characteristics summarized above. It can be used directly as a filler for a polymer matrix to impart electrical or improve thermal conductivity, to improve its mechanical properties, or as an additive to a fuel to enhance its combustion rate. For many other applications, the FGS powder may have to be used to prepare suspensions or inks to produce coatings for corrosion prevention, for electromagnetic shielding, tape-cast sheets as membranes, electrodes for batteries, and silk screening of iron-on patterns for electronic applications (Figure 14)[67] such as antennas as highlighted with numerous references in the introduction.

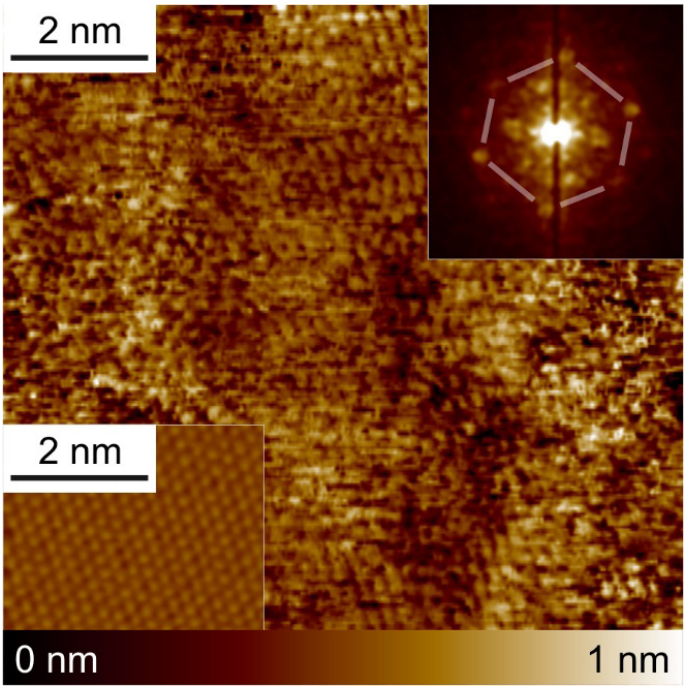

Figure 11.[40] **10 x 10 nm STM topography image of an FGS_{10}, taken at a bias voltage of 30 mV and a current of 5 nA. To minimize possible artifacts due to the size of the probe, the image was taken on top of a wrinkle of the sheet, where the topography is convex. The Fourier transform of the image shows that the hexagonal order is present (inset on the right top). The inset on the left bottom shows an STM image of HOPG taken under identical conditions (same topography color map than main image).**

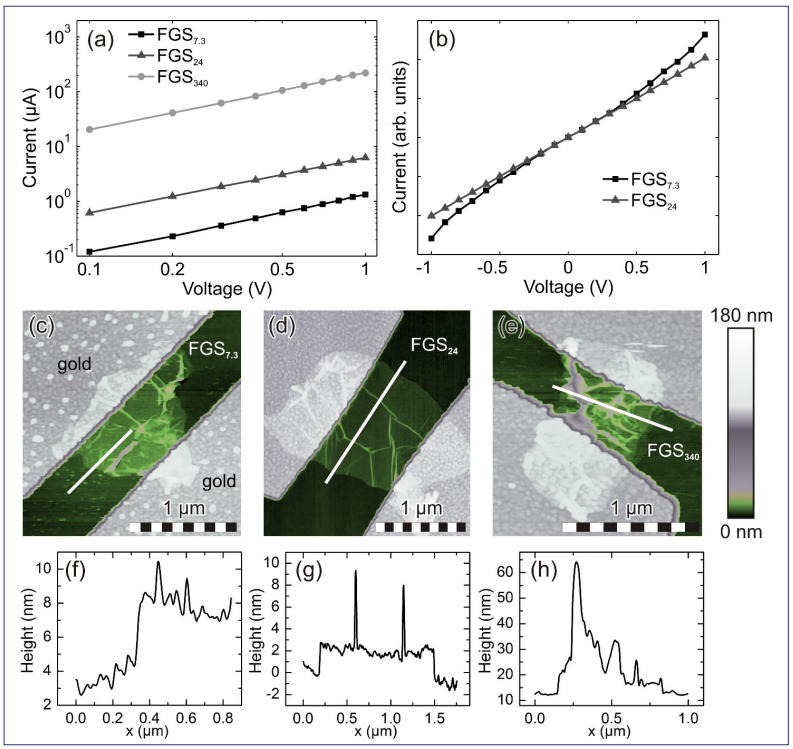

Figure 12.[49] **(a) I/V curves for three representative FGSs. (b) Non-linear response of $FGS_{7.3}$ compared to linear response of FGS_{24}, curves are normalized with respect to the slope at 0 V. (c-e) AFM topography images of the FGSs corresponding to (a). (f-h) Cross-sections along the lines in (c-e).**

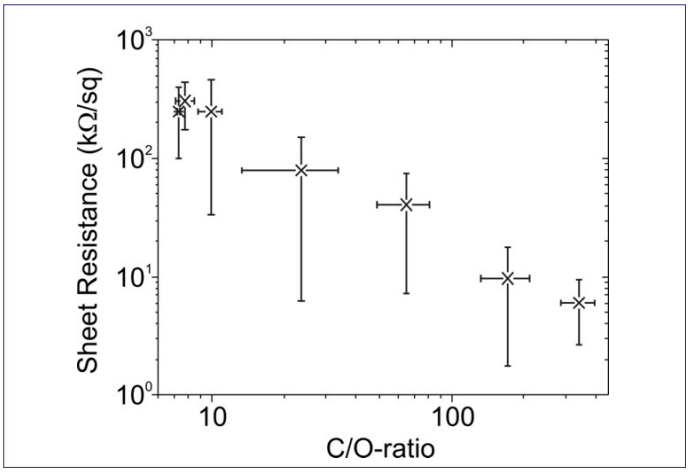

Figure 13.[49] **Compilation of data from a total of 25 sheets characterized with the 2-probe technique.**

The work presented so far was to demonstrate the complementary role of FGS vs. pristine graphene. In the following sections, I will demonstrate this complementary role with two unique applications: (i) a catalytic additive for the enhanced combustion of liquid fuels, and (ii) an energy storage material in supercapacitors. For many other applications, I refer to the publications cited in the introductory comments of the manuscript.

Fuel Combustion: The success of many future high-speed propulsion systems will depend on the ability to use environmentally friendly liquid fuels that offer high energy density, high heat sink capacity, short ignition delays, high reaction rates, and low cost.[24,25] Towards this goal, low concentrations of nanometer sized oxide particles dispersed within liquid hydrocarbon fuels show improved ignition and enhanced performance characteristics.[24,25] The colloidal particles, which are dispersed within the fuel during storage and handling, can facilitate endothermic fuel characteristics in the fuel delivered to the engine (i.e., as a liquid fuel catalyst) and then can be used to enhance ignition and combustion once the fuel is vaporized and appropriately mixed. A colloidal catalyst dispersed in the fuel is particularly appealing because it can be readily integrated into the liquid combustion systems.

Figure 14. FGS-based (commercial name Vor-x) inks are now being used to produce flexible printed electronics devices. (Vorbeck Materials Corp.)

Anticipating that FGS would also function as catalytic additive, we compared the performance of FGS_{22} against the commonly used oxide particles (Figure 15).[24] We used nitromethane (CH_3NO_2 or NM) as a highly energetic liquid organic nitro compound. NM has long been identified as a potential rocket propellant for various applications and is receiving renewed interest as a low toxicity alternative to highly toxic propellants such as hydrazine. As the simplest organic nitro compound, NM also serves as a surrogate for more complex energetic materials. Due to NM's low oxygen content and reactivity, NM behaves as a fuel at low pressures but requires additional oxidizers to sustain combustion.

Figure 15 demonstrates significant advantages to using the FGS_{22} rather than oxide nanoparticles.[24] Enhancements in burning rates due to FGS addition are much greater, with up to 175% increases over the burning rate of the monopropellant under lower pressure conditions.[24] At higher pressures, neat NM burning times are essentially equivalent to those of the colloid with 0.2 wt % FGS. Thus, the colloid additive of FGS_{22} not only enhances the burning rate of NM significantly but also causes the NM burning process to display less pressure sensitivity over the range of pressures considered, which is important for propulsion applications such as rocket motors, where pressure instabilities lead to reduced motor control and performance.

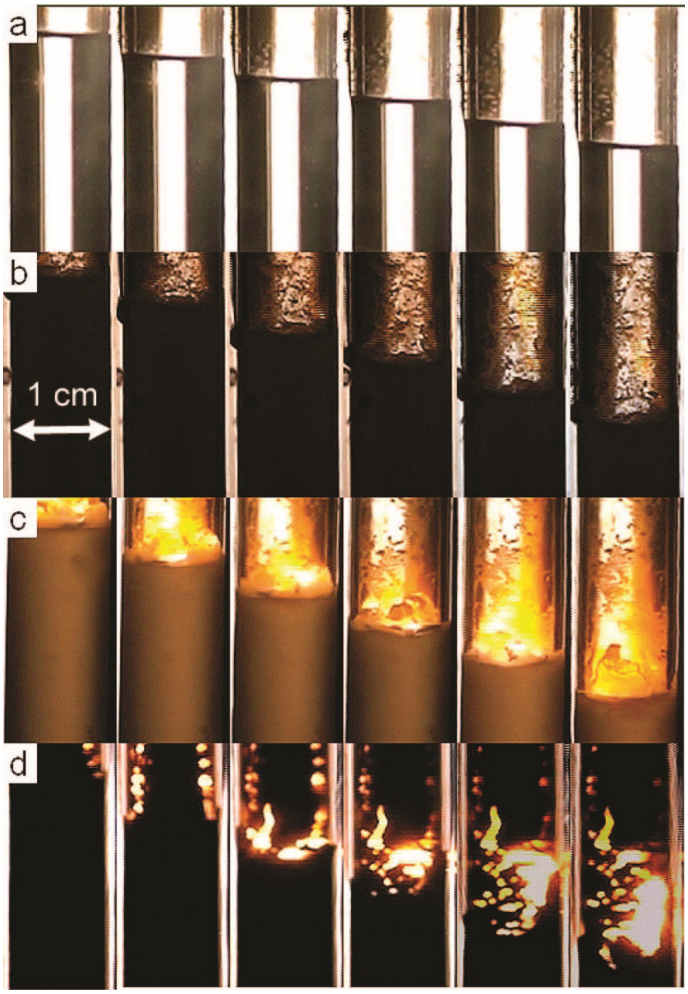

Figure 15.[24] **The images of regression process during combustion of nitromethane at 2 s intervals. (a) Neat nitromethane at 5.23 MPa, burning rate, r_b = 1.2 mm/s. (b) NM containing 0.5 wt % aluminum monohydroxide (AlOOH) at 5.16 MPa, r_b = 1.6 mm/s. (c) NM containing 0.39 wt % porous SiO_2 nanoparticles at 5.25 MPa, r_b = 1.9 mm/s. (d) NM containing 0.3% by mass FGS_{22} at 5.16 MPa, r_b = 2.2 mm/s. The fastest burn rate is achieved under roughly equivalent pressure through the addition of the smallest additive mass when using FGS_{22}. The residue left on the silica glass tube walls is much more apparent with FGS than the oxide materials, obscuring the view of much of the burning process; however, under fuel lean conditions much of the FGS would be consumed though oxidation processes.**

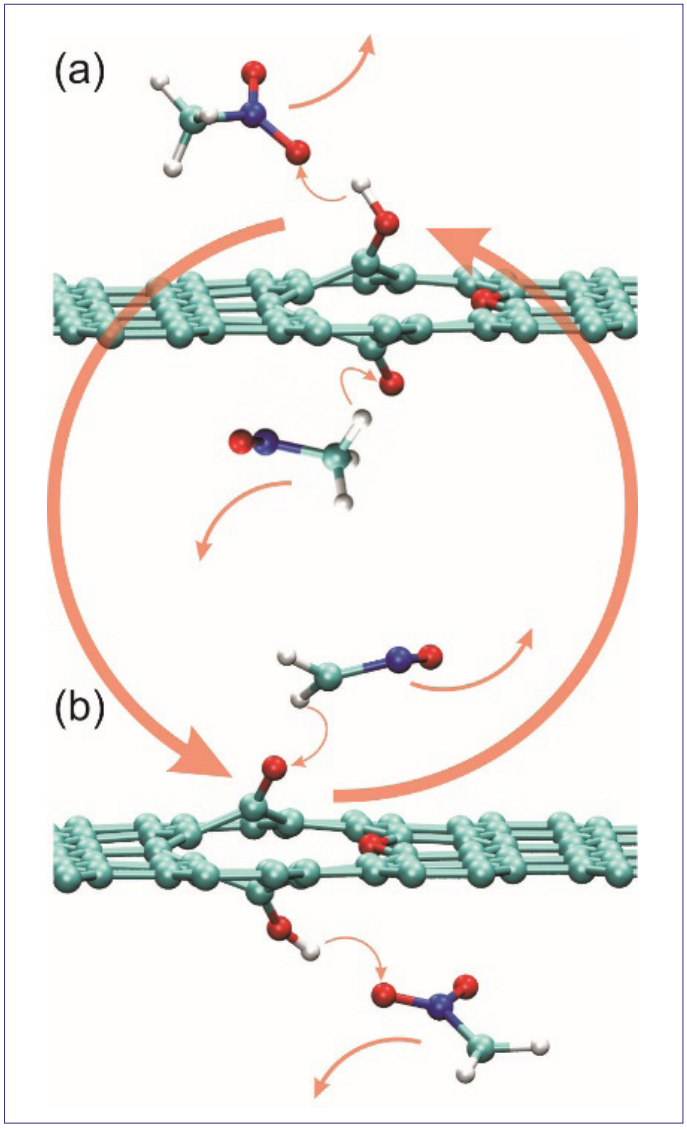

Figure 16.[25] **Catalytic role of the FGS in the decomposition reaction of NM. (a) An example of a proton transfer from a hydroxyl group on an FGS to a NM molecule, forming a reactive intermediate. (b) The subsequent regeneration of the hydroxyl group caused by a proton transfer from (in this example) an NM derivative to a carbonyl on the FGS. Other examples of proton transfer mechanisms are shown below the basal plane, representing a small sampling of the potential reactions occurring between FGS and NM and FGS and NM derivatives.**

To understand the catalytic mechanisms, we used ab initio molecular dynamics modeling, showing that carbon vacancy defects within the plane of the FGSs, functionalized with oxygen-containing groups, greatly accelerate the thermal decomposition of NM and its derivatives.[25] This occurs through reaction pathways involving the exchange of protons or oxygens between the oxygen-containing functional groups and NM and its derivatives (Figure 16)[25]. FGS initiates and promotes the decomposition of the monopropellant and its derivatives, ultimately forming H_2O, CO_2, and N_2. Concomitantly, oxygen-containing functional groups on the FGSs are consumed and regenerated without significantly changing the FGSs in accordance with experiments indicating that the FGSs are not consumed during combustion.

Supercapacitors:

While pristine graphene and FGSs share many similarities, such as high specific surface area (SSA), 2D morphology, and can exhibit high electrical conductivity,[49] they should not be expected to perform the same in applications due to the differences in the FGSs detailed in the previous sections. Unfortunately, this point is overlooked or misrepresented frequently in publications. Application in supercapacitors is one of these cases. Due to its potentially high SSA for capacitive charging, graphene has been presented as one of the most promising materials for next-generation supercapacitors. That is true for FGS but not for pristine graphene.[14]

Pristine graphene is not the best choice simply because its low quantum capacitance (C_Q) limits the double-layer capacitance (C_{DL})

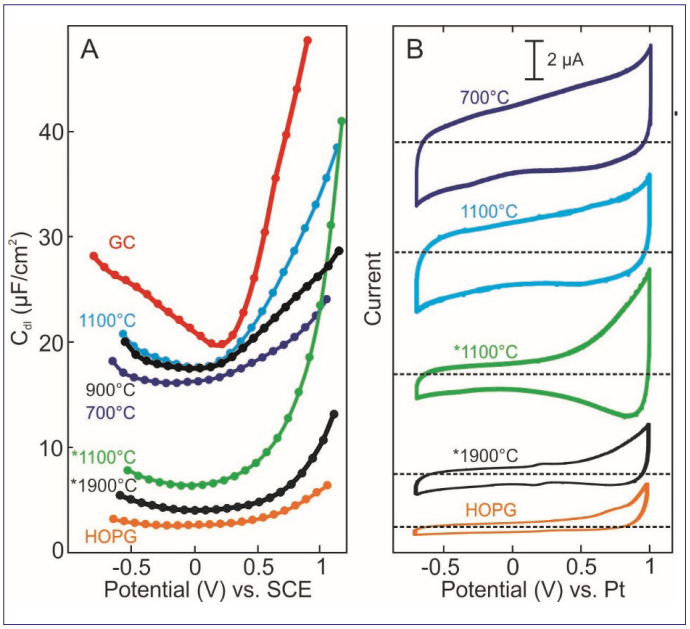

Figure 17.[14] Electrochemical behavior of FGS monolayers in 0.1 M TEABF4 in acetonitrile. Films were deposited after thermal exfoliation for 60 s or annealing (*) for 1 h at the indicated temperature. (a) CVs carried out at 100 mV/s between -0.5 and 0.5 V vs. Pt wire. After each measurement the Pt potential was estimated by adding ferrocene to the cell and carrying out CVs. (b) Capacitance measured by EIS at 100 Hz and 10 mV amplitude. The geometric surface area was estimated by analyzing the dependence of the peak current for ferrocene as a function of scan rate and the relative coverage of FGSs on each electrode was estimated by averaging over at least four different SEM images of monolayers on Au.

of the graphene/electrolyte interface to a low value.[14] This is in spite of the fact this limitation has been known for the basal-plane of graphite for almost five decades.[68] Consistent with this limitation, much of the supercapacitor research implies the use of pristine graphene but, in contrast, uses a functionalized and defective graphene formed through the reduction of graphene oxide, without clarifying why reduced graphene oxide is needed to achieve high capacitance. Figure 17[14] displays the differences. An optimal level of functionalization and lattice disorder in FGS yields a four-fold increase in C_{DL} over that of pristine graphene, suggesting graphene-based materials can indeed be tailored to produce electrodes with significantly higher gravimetric capacitance limits exceeding 450 F/g than what had been achieved (~ 274 F/g), even in non-aqueous electrolytes capable of high voltage operation. Theoretical work has also demonstrated that defects and functional groups can significantly increase graphene's density of states. Simulations of double-layer capacitance suggest that this can lead to significant enhancement.[69,70]

Figure 17A shows the C_{DL} values for monolayers prepared from several types of FGSs, determined by electrochemical impedance spectroscopy (EIS), as a function of frequency and potential.[14] For comparison, the results for glassy carbon (GC) and HOPG are also shown and agree with previous studies.[10,71] In particular, the capacitance-potential (*C-E*) curves for HOPG demonstrate the well-known, U-shaped dependence of C_{DL} on the electrode potential with a capacitance minimum (C_{min}) between 3 and 4 μF/cm². For GC, the shape of the *C-E* curves is dictated by the charge, size and orientation of the ions in the Helmholtz layer, all of which vary with potential. As the exfoliation temperature increases, the *C-E* curves of FGS approach those of GC. Conversely, annealing at temperatures much higher than 1100°C significantly reduces C_{DL}, with FGS approaching the performance of HOPG. An intermediate case arose for FGSs annealed for 2 h at 1100 °C. In this case the C_{min} is drastically reduced compared to the C_{min} of the material only exfoliated at 1100 °C but exhibits enhanced capacitance at high positive potentials suggesting an asymmetric doping in this FGS. Notice that this annealing-time dependent behavior coincides with the sharp decrease in the ID/IG Raman spectroscopy data and the sudden increase in the C/O observed (Figure 10B) at about the same temperature, demonstrating how critical it is to understand the role of the topological and the lattice defects on the properties. Using the same FGS materials while the sheet resistance continues to decrease with increasing C/O (Figure 13), an optimal point in C_{DL} is reached at a critical C/O.

As shown in Figure 17B, the CVs are nearly rectangular in shape except for the case where FGSs were annealed at 1100 °C for 2 h. The relative magnitudes of the capacitive current in the CVs are commensurate with the measurements carried out by EIS. The shape of the CVs, the relatively constant capacitance with measurement frequency (independent of DC potential), and the fact that the measurements are carried out in an aprotic electrolyte all indicate that the electrodes can be considered ideally polarizable and the capacitance due to Faradaic contributions is negligible.

These results demonstrate how by tailoring the structure and chemistry of FGSs, it is possible to achieve capacitances 3 to 4 times higher than that of HOPG and what has been observed for pristine graphene.

Prospects

Excitement that started with the studies on pristine graphene revealing its unprecedented charge carrier mobility at room temperature paved the way for most of the work on functionalized graphene described in this review. The wide application range indicated for FGS is surely not limited to the examples described and/or referenced here. FGS is a complementary material to pristine graphene where in some applications specific forms of FGS are the right choice due to the advantages provided by its functionalization and defective structure. In addition to FGS' unique advantages in some applications, it is important to recognize that its availability in industrial quantities provides a major advantage in product development. Some products on flexible electronics and composite materials are already out. What seems to be blocking the development of commercial products at a faster pace is the complexities of maneuvering around the market forces, not the lack of scientific knowledge.

Acknowledgements

The work summarized in this manuscript represents the contributions of many colleagues at Princeton University, Vorbeck Princeton Research Center, and many other collaborating institutions. Their names and affiliations are indicated in the references provided below. I am very grateful for their contributions. The initial project was initiated under a grant from NASA. Additional support from the National Science Foundation, Air Force Office of Scientific Research, Department of Energy, and the Army Research Office kept the work going. Specific funding sources are indicated in our papers cited.

I declare conflict of interest position as a founder and a board member of Vorbeck Materials Corp., Jessup, Maryland USA that manufactures FGS under the trade name Vor-x.

References

1. A.K. Geim and K.S. Novoselov, *Nat. Mater.* **6**, 183 (**2007**).
2. H.C. Schniepp, J.L. Li, M.J. McAllister, H. Sai, M. Herrera-Alonso, D.H. Adamson, R.K. Prud'homme, R. Car, D.A. Saville, and I.A. Aksay, *J. Phys. Chem. B* **110**, 8535 (**2006**).
3. M.J. McAllister, J.L. Li, D.H. Adamson, H.C. Schniepp, A.A. Abdala, J. Liu, M. Herrera-Alonso, D.L. Milius, R. Car, R.K. Prud'homme, and I.A. Aksay, *Chem. Mater.* **19**, 4396 (**2007**).
4. S. Stankovich, D.A. Dikin, R.D. Piner, K.A. Kohlhaas, A. Klinehammes, Y. Jia, Y. Wu, S.T. Nguyen, and R.S. Ruoff, *Carbon* **45**, 1558 (**2007**).
5. T. Ramanathan, A.A. Abdala, S. Stankovich, D.A. Dikin, M. Herrera-Alonso, R.D. Piner, D.H. Adamson, H.C. Schniepp, X. Chen, R.S. Ruoff, S.T. Nguyen, I.A. Aksay, R.K. Prud'homme, and L.C. Brinson, *Nat. Nanotechnol.* **3**, 327 (**2008**).
6. B. Ozbas, C.D. O'Neill, R.A. Register, I.A. Aksay, R.K. Prud'homme, and D.H. Adamson, *J. Polym. Sci., Part B: Polym. Phys.* **50**, 910 (**2012**).
7. M.D. Stoller, S. Park, Y. Zhu, J. An, and R.S. Ruoff, *Nano Lett.* **8**, 3498 (**2008**).
8. D. Wang, D. Choi, J. Li, Z. Yang, Z. Nie, R. Kou, D. Hu, C. Wang, L. Zhang, I.A. Aksay, and J. Liu, *ACS Nano* **3**, 907 (**2009**).
9. D. Wang, R. Kou, D. Choi, Z. Yang, Z. Nie, J. Li, L.V. Saraf, D. Hu, J. Zhang, G.L. Graff, J. Liu, M.A. Pope, and I.A. Aksay, *ACS Nano* **3**, 1587 (**2010**).
10. M.A. Pope, C. Punckt, and I.A. Aksay, *J. Phys. Chem. C* **115**, 20326 (**2011**).
11. Y. Cao, X. Li, I.A. Aksay, J. Lemmon, Z. Nie, Z. Yang, and J. Liu, *Phys. Chem. Chem. Phys.* **13**, 7660 (**2011**).
12. J. Xiao, D. Mei, X. Li, D. Wang, G.L. Graff, W.D. Bennett, Z. Nie, L.V. Saraf, I.A. Aksay, J. Liu, and J.G. Zhang, *Nano Lett.* **11**, 5071 (**2011**).
13. A.G. Hsieh, C. Punckt, and I.A. Aksay, *J. Electrochem. Soc.* **162**, A1566 (**2015**).
14. M.A. Pope and I.A. Aksay, *J. Phys. Chem. C* **119**, 20369 (**2015**).
15. M.A. Pope and I.A. Aksay, *Adv. Energy Mat.* **5**, 1500124 (**2015**).
16. H. Wu, J, Wang, X. Kang, C. Wang, D. Wang, J, Liu, I.A. Aksay, and Y. Lin, *Talanta* **80**. 403 (**2009**).
17. X. Kang, J. Wang, H. Wu, I.A. Aksay, J. Liu, and Y. Lin, *Biosensors and Bioelectronics* **25**, 901 (**2009**)
18. Y. Shao, J. Wang. H. Wu, J. Liu, I.A. Aksay and Y. Lin, *Electroanalysis* **22**, 1027 (**2010**).
19. C. Punckt, M.A. Pope, J. Liu, Y. Lin, and I.A. Aksay, *Electroanalysis* **22**, 2834 (**2010**).
20. J.D. Roy-Mayhew, D.J. Bozym, C. Punckt, and I.A. Aksay, *ACS Nano* **4**, 6203 (**2010**).
21. J.D. Roy-Mayhew, G. Boschloo, A. Hagfeldt, and I.A. Aksay, *ACS Appl. Mater. Interfaces* **4**, 2794 (**2012**).
22. J.D. Roy-Mayhew and I.A. Aksay, *Chem. Rev.* **114**, 6323 (**2014**).
23. J.D. Roy-Mayhew, M.A. Pope, C. Punckt, and I.A. Aksay, *ACS Appl. Mater. Interfaces* **8**, 9134 (**2016**).
24. J.L. Sabourin, D.M. Dabbs, R.A. Yetter, F.L. Dryer, and I.A. Aksay, *ACS Nano* **3**, 3945 (**2009**).
25. L.M. Liu, R. Car, A. Selloni, D.M. Dabbs, and I.A. Aksay, *J. Am. Chem. Soc.* **134**, 19011 (**2012**).
26. H.S. Sim, R.A. Yetter, T.L. Connell, D.M. Dabbs, and I.A. Aksay, *Combust. Sci. Technol.* **192**, 1420 (**2020**).
27. H.S. Sim, R.A. Yetter, S. Hong, A.C.T. van Duin, D.M. Dabbs, and I.A. Aksay, *ACS Appl. Energy Mater.* **3**, 7637 (**2020**).
28. H.S. Sim, R.A. Yetter, S. Hong, A.C.T. van Duin, D.M. Dabbs, and I.A. Aksay, *Combust. Flame* **217**, 212 (**2020**)
29. A.G. Hsieh, C. Punckt, S. Korkut, and I.A. Aksay, *J. Phys. Chem. B* **117**, 7950 (**2013**).
30. A.G. Hsieh, S. Korkut, C. Punckt, and I.A. Aksay, *Langmuir* **29**, 14831 (**2013**).
31. M. Alifierakis, K.S. Sallah, I.A. Aksay, J.H. Prévost, *AIChE J.* **63**, 5462 (**2017**).
32. S. Korkut, J.D. Roy-Mayhew, D.M. Dabbs, D.L. Milius, and I.A. Aksay, *ACS Nano* **5**, 5214 (**2011**).
33. L. Xu, L. Wang, W. W. Zhang, J. Xue, and S. Hou, *ACS Omega* **7**, 10955 (**2022**).
34. Y. Chen, J. Li, T. Li, L. Zhang, and F. Meng, *Carbon* **180**, 163 (**2021**).
35. C. Pavlou, M.G.P. Carbone, A.C. Manikas, G. Trakakis, C. Koral, G. Papari, A. Andreone, C. Galiotis, *Nat. Communications* **12**, 4655 (**2021**).
36. K. Ollik, J. Karczewski, J. Lieder, *Materials* **14**, 1410 (**2021**).
37. S. Böhm, *Nat. Nanotechnol.* **9**, 741 (**2014**).
38. J. Zhang, R. Song, X. Zhao, R. Fang, B. Zhang, W. Qian, J. Zhang, C. Liu, and D. He, *ACS Omega* **5**, 12937 (**2020**).
39. A. Scott, *C&ENews* **94**, Issue 15 (**2016**).
40. K.N. Kudin, B. Ozbas, H.C. Schniepp, R.K. Prud'homme, I.A. Aksay, and R. Car, *Nano Lett.* **8**, 36 (**2008**).
41. A. Bagri, C. Mattevi, M. Acik, Y.J. Chabal, M. Chhowalla, and V. B. Shenoy, *Nat. Chem.* **2**, 581 (**2010**).
42. B.C. Brodie, *Phil. Trans. Roy. Soc. London* **149**, 249 (**1859**); B.C. Brodie, *Ann. Chem. Liebigs* **114**, 6 (**1860**).
43. H.P. Boehm, *Angew. Chem. Int. Ed.* **49**, 9332 (**2010**).
44. L. Staudenmaier, *Ber. Dtsch. Chem. Ges.* **31**, 1481 (**1898**).
45. J.D. Bernal, *Proc. Roy. Soc. A* **106**, 749 (**1924**).
46. W.S. Hummers and R.E. Offeman, *J. Am. Chem. Soc.* **80**, 1339 (**1958**).
47. D.C. Marcano, D.V. Kosynkin, J.M. Berlin, A. Sinitskii, Z.Z. Sun, A. Slesarev, L.B. Alemany, W. Lu, and J.M. Tour, *ACS Nano* **4**, 4806 (**2010**).
48. H.P. Boehm, A. Clauss, G. Fischer and U. Hofmann, in *Proc. 5th Bieniel. Conference on Carbon, Vol. 2. Pergamon Press, Oxford*, **1962**, p. 73.
49. C. Punckt, F. Muckel, S. Wolff, I.A. Aksay, C.A. Chavarin, G. Bacher, and W. Mertin, *Appl. Phys. Lett.*, **102**, 023114 (**2013**).
50. K.S. Novoselov, A.K. Geim, S.V. Morozov, D. Jiang, Y. Zhang, S.V. Dubonos, I.V. Grigorieva, and A.A. Firsov, *Science* **306**, 666 (**2004**).
51. M. Hirata, T. Gotou, S. Horiuchi, M. Fujiwara, and M. Ohba, *Carbon* **42**, 2929 (**2004**).
52. W. Scholz and H.P. Boehm, *Z. Anorg. Allg. Chem.* **369**, 327 (**1969**).
53. A. Dimiev, D.V. Kosynkin, L.B. Alemany, P. Chaguine, and J.M. Tour, *J. Am. Chem. Soc.* **134**, 2815 (**2012**).
54. I. Jung, D.A. Dikin, R.D. Piner, and R.S. Ruoff, *Nano Lett.* **8**, 4283 (**2008**).
55. D.R. Dreyer, S. Park, C.W. Bielawski, and R.S. Ruoff, *Chem. Soc. Rev.* **39**, 228 (**2010**).
56. X.S. Du, M. Xiao, Y.Z. Meng, and A.S. Hay, Carbon **43**, 195 (**2005**).
57. A. Lerf; H. He, M. Forster, J. Klinowski, *Phys. Chem. B* **102**, 4477 (**1998**)
58. J.L. Li, K.N. Kudin, M.J. McAllister, R.K. Prud'homme, I.A. Aksay, R. Car, *Phys. Rev. Lett.* **96**, 176101 (**2006**).
59. S. Pan and I.A. Aksay, *ACS Nano* **5**, 4073 (**2011**).
60. M.D. Thouless, Z. Li, N.J. Douville, S. Takayama, *J. Mech. Phys. Solids*, **59**, 1927 (**2011**).
61. H.C. Schniepp, K.N. Kudin, J.L. Li, R.K. Prud'homme, R. Car, D.A. Saville, and I.A. Aksay, *ACS Nano* **2**, 2577 (**2008**).
62. G.D. Lee, C.Z. Wang, E. Yoon, N.M. Hwang, D.Y. Kim, K.M. Ho, *Phys. Rev. Lett.* **95**, 205501 (**2005**).
63. A.J.Stone and D.J Wales, *Chem. Phys. Lett.* **128**, 501 (**1986**).
64. A.C. Ferrari, J. Robertson, *J. Phys. Rev. B* **61**, 14095 (**2000**).
65. F. Tuinstra and J.L. Koenig, *J. Chem. Phys.* **53,** 1126 (**1970**).
66. M.A. Pope, S. Korkut, C. Punckt, and I.A. Aksay, *J. Electrochem. Soc.* **160**, A1653 (**2013**).
67. M.S. Reisch, *C&ENews* **91**, Issue 1, (**2013**).
68. J.P. Randin, E. Yeager, *J. Electroanal. Chem. Interfacial Electrochem.* **58**, 313 (**1975**).
69. A.J. Pak, E. Paek, and G.S. Hwang, *Carbon* **68**, 734 (**2014**).
70. A.J. Pak, E. Paek, and G.S. Hwang, *J. Phys. Chem. C* **118**, 21770 (**2014**).
71. D.J.Bozym, B. Uralcan, D.T. Limmer, M.A. Pope, N.J. Szamreta, P.G. Debenedetti, I.A. Aksay, *J. Phys. Chem. Lett.* **6**, 2644 (**2015**).